



Halite-structured (MgCoNiMnFe)O_x high entropy oxide (HEO) for chemical looping dry reforming of methane

Yu Shao^{a,b}, Chao Wu^c, Shibo Xi^{c,*}, Preston Tan^a, Xianyue Wu^a, Syed Saqline^a, Wen Liu^{a,b,**}

^a School of Chemistry, Chemical Engineering and Biotechnology, Nanyang Technological University, 62 Nanyang Drive, Singapore 637459, Singapore

^b Cambridge Centre for Advanced Research and Education in Singapore, 1 CREATE Way, Singapore 138602, Singapore

^c Institute of Sustainability for Chemicals, Energy and Environment (ISCE²), Agency for Science, Technology and Research (A*STAR), 1 Pesek Road, Jurong Island, Singapore 627833, Singapore

ARTICLE INFO

Keywords:

High entropy oxides
Chemical looping
Dry reforming of methane

ABSTRACT

The configurational disorder of high entropy oxides (HEOs) promotes the reversible exsolution–redissolution of constituent metal species. This unique feature could be exploited to facilitate cyclic lattice oxygen storage and exchange. Herein, we report an *in situ* generated, halite-structured (MgCoNiMnFe)O_x HEO, which simultaneously functions as a redox catalyst and an oxygen carrier for dry reforming of methane in a chemical looping process (CL–DRM). Accordingly, the (MgCoNiMnFe)O_x/ZrO₂ HEO catalyst exhibits outstanding DRM activity, syngas selectivity and cyclic stability compared to medium-entropy oxides and bimetallic oxides over 100 CL–DRM cycles at 800 °C. XRD analysis verified the entropy-mediated preservation of the alloy/HEO/ZrO₂ catalytic structure over CL–DRM cycles. XAFS studies revealed the reversible and cyclic evolution–dissolution of Ni, Fe, Co over redox cycles. The exsolved NiFeCo nanoalloy exhibited high efficiency in activating CH₄. This study has demonstrated the potential applications of HEO-based catalysts in efficient chemical looping processes.

1. Introduction

In recent years, high entropy materials (HEMs) have attracted enormous research interests [1–3]. They refer to a class of materials with configurational entropy, $\Delta S_{conf} > 1.5 R$, where ΔS_{conf} of a n -component system with mole fractions x_i for the i^{th} component can be estimated as in Eq. 1. Assuming that the occupancies of the cationic sites by metal elements are completely random, ΔS_{conf} would be maximum when the values of x_i are all equal. Also, the configurational entropic driving force is more profound at higher temperatures. A broad library of HEMs has been designed and synthesized, including alloys [4–7], polymers [8], oxides [9,10], diborides [11], carbides [12], nitrides [13], sulfides [14], MOFs [15], hydroxides [16], di-chalcogenides [17], glasses [18], etc.

$$\Delta S_{conf} = -R \sum_{i=1}^n x_i \ln x_i \quad (1)$$

Amongst various HEMs, high entropy alloys (HEAs) and high entropy oxides (HEOs) have been extensively investigated in catalytic applications. HEAs have been prepared via various approaches including

carbon thermal shock [6], mechano-chemical synthesis [19], chemical deposition [20], flame synthesis [21], and wet chemical synthesis [22]. For instance, Hu and Wang et al. synthesized PtRhRuCe and CoMoFeNiCu HEAs/C as catalysts for thermo-catalytic ammonia combustion and decomposition, respectively [6,7]. Furukawa et al. synthesized PtCoNiSnInGa HEA/CeO₂, which exhibited decent catalytic performance in the oxidative propane dehydrogenation with CO₂ [23].

HEOs have also been studied for various catalytic applications since their first report in 2015 [9]. For instance, a 10-metal HfZrLaVCoTiNdGdYPdO HEO, prepared by carbothermal shock, found application in catalyzing oxygen reduction reactions [24]. The ultrahigh stability of the catalyst was attributed to the strengthened interfacial bonding which prevents nanoparticles detachment, as well as the high entropy effect which inhibits metal segregation [24]. In addition, the unique coordination environments in HEOs could render exquisite perturbation to electronic structures that are otherwise hard to access. For example, Seh and Xu et al. discovered that the high spin Co in MgCoNiCuZnO HEO catalyst facilitated the synergistic Cu–Co pairing, which is favored for electrochemical ammonia generation [25]. Schaak et al. revealed the

* Corresponding author.

** Corresponding author at: School of Chemistry, Chemical Engineering and Biotechnology, Nanyang Technological University, 62 Nanyang Drive, Singapore 637459, Singapore.

E-mail addresses: xi_shibo@isce2.a-star.edu.sg (S. Xi), wenliu@ntu.edu.sg (W. Liu).

<https://doi.org/10.1016/j.apcatb.2024.124191>

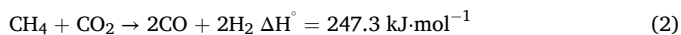
Received 6 March 2024; Received in revised form 2 May 2024; Accepted 9 May 2024

Available online 11 May 2024

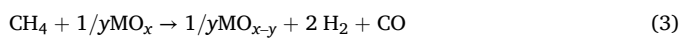
0926-3373/© 2024 Elsevier B.V. All rights reserved, including those for text and data mining, AI training, and similar technologies.

band gap narrowing in a (FeCoNiCuZn)Al₂O₄ catalyst relative to all its parent spinel oxides, giving rise to enhanced oxygen evolution reaction [26]. A dual-phase TiZrNbHfTaO₁₁ HEO prepared by mechanical alloying was applied in the photocatalytic reduction of CO₂ [27]. Furthermore, a CeZrHfTiLaO_x HEO has been demonstrated to stabilize single-atom Pd catalyst via the high entropy effect by Dai et al [28]. In another study, Co₃MnNiCuZnO_x HEO was prepared via a mechano-chemical redox-based method; it was demonstrated that the exsolved CuCoNi alloy tends to dissolve back to the oxide matrix, driven by the high configurational entropy of the HEO, thus mitigating the sintering of the metal particles [29]. In fact, this exsolution–dissolution mechanism is widely exploited as a means to regenerate the structures of reducible oxide supported metal catalysts, preventing sintering and rendering ultrahigh catalyst stability [30,31].

Dry reforming of methane (DRM, Eq. 2) is a promising pathway to simultaneously upgrade two greenhouse gases (CO₂ and CH₄) to syngas (CO + H₂), an important feedstock for bottom-up chemical synthesis, e. g. via Fischer–Tropsch process, methanol production, etc [32].



Unfortunately, the commercialization of the DRM process faces several challenges [33,34], including (i) side reactions such as the reverse water gas shift reaction preventing complete conversion of CO₂; (ii) coke formation and accumulation due to methane decomposition and the Boudouard reaction, leading to catalyst deactivation; (iii) sintering induced catalyst deactivation; (iv) reaction conversion and selectivity limited by thermodynamic equilibrium; and (v) the high endothermicity requiring input of high grade heat. In recent years, chemical looping–dry reforming of methane (CL–DRM) was proposed to tackle these issues by dividing DRM into the reforming (Eq. 3) and the regeneration (Eq. 4) reactions [33,34].



“MO_x” refers to an oxygen carrier that is cycled between two reactors and undergoes dynamic redox cycles. By splitting the reaction into two reactors, the thermodynamic limitations seen in conventional DRM reactors is inherently removed, leading to high CH₄ and CO₂ conversions [33]; while suppressing side reactions such as RWGS [33]. Moreover, by designing reactors to accommodate sufficient residence time during CO₂ oxidation (Eq. 4), cyclic coke removal can be realized, thereby eliminate the accumulation of carbon deposition. On the other hand, the design of redox catalysts is crucial to the development of an effective and efficient CL–DRM process [33]. In particular, an ideal redox catalyst (also as an oxygen carrier) for CL–DRM should have appropriate lattice oxygen activity, as well as high catalytic activity towards methane activation and CO₂ activation. Lattice oxygens that are overly active, such as those in NiO and Fe₂O₃, may lead to the undesired full oxidation of methane to CO₂ and H₂O [35,36], while insufficiently active lattice oxygens may result in excessive coking, which could not be effectively removed during oxidative regeneration (e.g. by CO₂) [33,37]. Therefore, it is essential to appropriately tune the lattice oxygen activity of the Fe-based redox catalysts. For example, doping LaFeO₃ with Al or Ga induced a structural distortion, leading to significant improvement in their syngas productivity in chemical looping reforming [38]. This apparent promotional effect is attributed to the formation of the asymmetric Fe–O–Al motif, which favors fast and selective partial oxidation of methane [36]. Furthermore, the cyclic degradation of redox catalysts, caused by sintering, coking and irreversible phase segregation are also challenges to be addressed in the development of redox catalysts for CL–DRM.

HEOs possess the natural advantage of versatile composition, which provides great degrees of freedom in tuning their lattice oxygen reactivity as well as catalytic activity [39,40]. In particular, the dynamic exsolution–dissolution of active species promoted by the high entropy

effect makes HEOs ideal redox catalysts for chemical looping applications [31,41]. Recently, a (Fe_{0.2}Mg_{0.2}Mn_{0.1}Al_{0.3}Cr_{0.2})₃O₄ spinel HEO prepared by wet chemistry was demonstrated to be an excellent redox catalyst for chemical looping–steam reforming of methane [42]. The high entropy effect was attested to prevent the host oxides from decomposing and sintering during the reforming stage and facilitated the dissolution of metal back to the HEO matrix during the regeneration stage [42]. The abovementioned work exemplifies the potential application of HEOs as a redox catalyst for chemical looping processes with outstanding cyclic durability and optimized lattice oxygen reactivity.

For chemical looping applications, reducible oxides of 3d transition metals with melting points above 800 °C (*viz.* Cr, Ni, Co, Mn, Fe and Cu) are typically used as oxygen carriers and redox catalysts. Among these oxide constituents, Co, Ni and Cu can readily adopt an oxidation state of 2+ and form a halite-structured solid solution. On the other hand, although the Shannon ionic radii and M²⁺–O bond lengths of Fe²⁺ and Mn²⁺ matches closely to those of Co²⁺, Ni²⁺ and Cu²⁺, the local mixing enthalpies of Fe²⁺ and Mn²⁺ with the other divalent metal oxides in the halite structure were predicted, by DFT calculations, to be beyond the compensation of high entropy effect, primarily owing to the low stability of Fe²⁺ and Mn²⁺ in air [43]. Therefore, the incorporation of Fe and Mn into a HEO consisting primarily of 3d metals would involve preparing a spinel structured solid solution, as done by Wang et al [42].

Nevertheless, we demonstrate in this work that a (MgCoNiMnFe)O_x halite-phase HEO can be formed *in situ* during CL–DRM cycles (Fig. 1). This is because the redox environment of CL–DRM exerts an external driving force to facilitate the formation of the halite-structured HEO. The obtained (MgCoNiMnFe)O_x well inherited unique features of HEOs such as promoting exsolution–dissolution of Ni, Fe, Co species in and out of the HEO matrix. These redox active species simultaneously serve as the catalytic active sites and the oxygen carriers to facilitate the transport of lattice oxygen. The HEO catalyst afforded a high selectivity towards partial oxidation of methane, a high catalyst durability and high activity towards both methane and CO₂ conversion over CL–DRM cycles.

2. Experimental section

2.1. Preparation of redox catalysts

Catalysts presented in this work (HEO, HEO/ZrO₂, MEO/ZrO₂, NiFeO_x/ZrO₂, and NiFeO_x/Al₂O₃) were prepared via a simple coprecipitation method [44], followed by a two-stage calcination treatment. In a typical synthesis, 100 mL of aqueous solution containing 0.1 M metal cations (*i.e.* total cationic concentration, Table S1) was injected into 100 mL of NaOH aqueous solution at a rate of 20 mL·min^{−1} under stirring. Mg(NO₃)₂, Co(NO₃)₂, Ni(NO₃)₂, Mn(NO₃)₂, Fe(NO₃)₃, ZrCl₄, and Al(NO₃)₃ precursors were used. The mixture was stirred for another 10 min and aged at ambient conditions for 3 h. The precipitates were collected via centrifugation and washed first with water, then with ethanol. The obtained precipitates were dried at 70 °C for 3 h, followed by calcination at 500 °C for 2 h (heating rate 10 °C·min^{−1}) and cooled down naturally. A second calcination was performed at 900 °C for 2 h (heating rate 10 °C·min^{−1}); the catalyst was air quenched. The obtained catalysts were sieved to 150–250 μm in size.

2.2. Chemical looping–dry reforming of methane

The CL–DRM reaction was carried out in a fixed bed reactor. In a typical experiment, 200 mg of the prepared catalyst (150–250 μm) was filled into a tube (recrystallized alumina, 500 mm in length, O.D. 10 mm, I.D. 8 mm) packed with alumina sands and quartz wool. The catalyst zone was heated to 800 °C (heating rate 10 °C·min^{−1}) in an Ar flow of ca. 200 sccm. Thereafter, the total flow rate was kept at ca. 200 sccm. 10 sccm (5 %) of He was injected as an internal standard to track changes in the flow rate. In each CL–DRM cycle, the feed gases were switched in the following order: 5 % CH₄/ 5 % He/ 90 % Ar for 2 min,

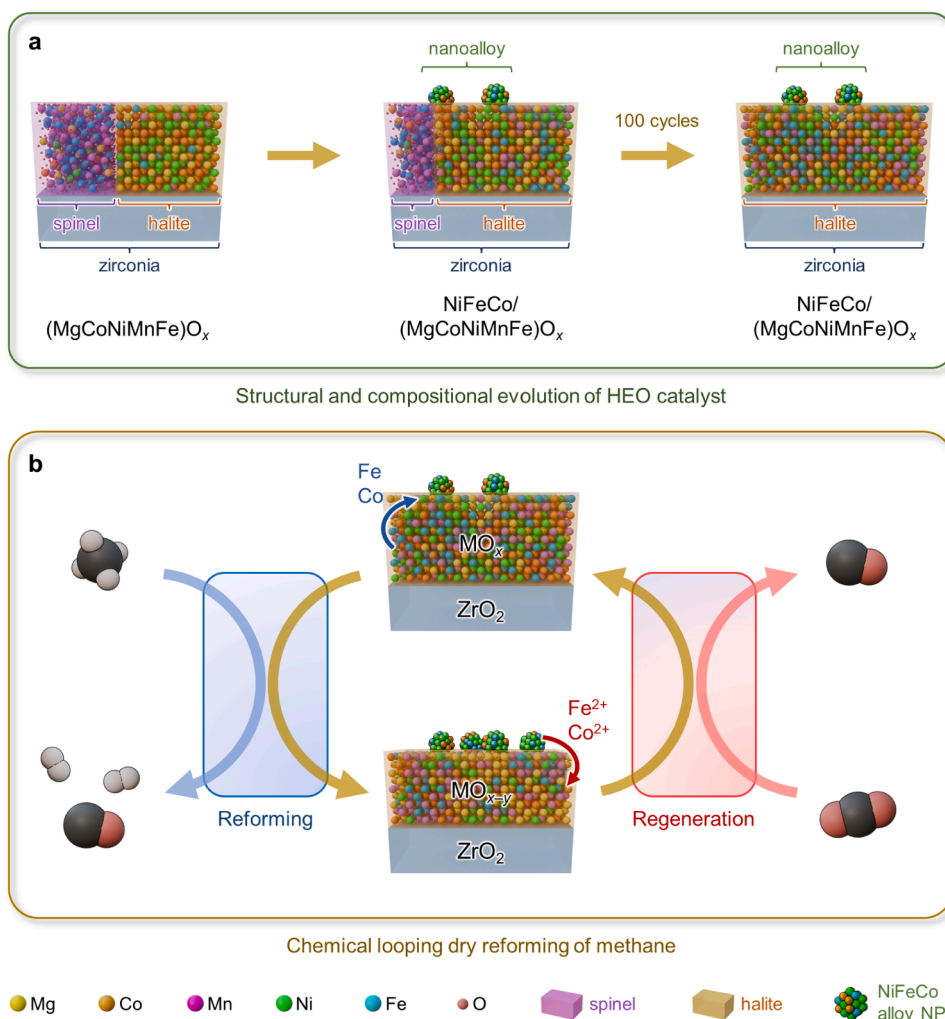


Fig. 1. Schematic illustrations of (a) the structural and compositional evolution of the $(\text{MgCoNiMnFe})\text{O}_x$ catalyst from its freshly calcined state, i.e. a biphasic spinel–halite, to its equilibrium state, i.e. nanoalloys supported on halite–HEO. (b) Schematic illustrations of the chemical looping dry reforming of methane process facilitated by the exsolution–dissolution of Fe and Co species from and into the halite structured HEO.

5 % He/ 95 % Ar for 2 min, 10 % CO_2 / 5 % He/ 85 % Ar for 5 min, and 5 % He/ 95 % Ar for 2 min. These steps represent CH_4 reforming, purging, regeneration and purging, respectively. Each sample was tested isothermally at 800 °C for 100 CL–DRM cycles. The effluent gas composition was monitored with a HIDEN QGA Quantitative Gas Analyzer (HAS-301–1379B).

2.3. Catalyst characterization

The crystallographic structures of the redox catalysts were investigated by X-Ray diffraction (XRD) with a Bruker D2 Phaser diffractometer under ambient conditions ($\text{Cu K}\alpha 1 = 1.5406 \text{ \AA}$). The obtained XRD patterns were analyzed by Rietveld refinement using GSAS/EXPGUI software [45]. Morphological and compositional information was obtained with field emission transmission electron microscope (FETEM, JEM-2100 F) and field emission scanning electron microscopy (FESEM, JSM-7200 F). N_2 physisorption experiments were conducted with a Micromeritics ASAP 2460 instrument, after degassing the samples at 120 °C for 12 h. Raman spectra of the catalysts were acquired with a HORIBA Scientific LabRAM HR Evolution instrument with an excitation wavelength of 514 nm. Compositional information was obtained with an Agilent 5800 ICP–OES and a Bruker S8 TIGER XRF instrument. Lattice oxygen reactivity was determined with temperature-programmed reduction in H_2 (H_2 –TPR), performed with a Micromeritics AutoChem

II 2920 instrument. X-ray photoelectron spectroscopy (XPS) data were obtained with a Kratos AXIS Supra spectrometer (Al $\text{K}\alpha$ source, 1846.6 eV). X-ray absorption fine structure (XAFS) spectra were collected at the XAFCA beamline of the Singapore Synchrotron Light Source [46], under transmission mode, in ambient conditions. Metallic Co, Ni, Fe foils and Mn powder were used for spectral calibration. The XAFS data were processed with Demeter software [47].

3. Results and discussion

3.1. Design and synthesis of $(\text{MgCoNiMnFe})\text{O}_x$ HEO

In a previous study, halite structured 3d metal HEO with the nominal formula $(\text{MgCoNiCuZn})\text{O}$ has been synthesized [9]. Here, MgO is expected to act as a structural promoter [42,48], Ni and Co could provide activities towards C–H activation [49,50], while Cu could contribute functionality towards H_2 activation and RWGS reaction [51]. However, the presence of Zn in the $(\text{MgCoNiCuZn})\text{O}$ HEO is unfavored owing to its low melting point and boiling point (at 420 °C and 907 °C, respectively) and therefore must be avoided in high temperature applications such as DRM, which is typically carried out above 800 °C. Substituting Cu and Zn with trivalent metal cations such as Al^{3+} would lead to the formation of spinel phases, while divalent metal cations with mismatching ionic radius such as Ca^{2+} may result in the formation perovskite structures. In

both spinel and perovskite solid solutions, metal cations of Co, Fe and Mn tend to adopt trivalent or even higher oxidation states. The former has been recently reported by Wang et al [42]. In contrast, in a halite structured HEO, e.g. (MgCoNiMnFe) O_x , the high configurational entropy offers a possibility to stabilize Co, Fe and Mn at lower oxidation states, offering unique redox activities that are not accessible via spinel or perovskite phases. Therefore, in the present study we formulate a (MgCoNiMnFe) O_x HEO for the potential application of CL-DRM. We note that there has not been any prior report of such halite structured (MgCoNiMnFe) O_x HEO.

(Mg_{0.2}Co_{0.2}Ni_{0.2}Mn_{0.2}Fe_{0.2}) O_x (denoted as HEO hereafter for brevity) was prepared via a simple coprecipitation followed by two-stage calcination. Although the sample was quenched rapidly with air, the quenched sample exhibited segregated halite (86 %, molar, metal basis) and spinel (14 %) phases (Figure S1 and Table S2), in line with computational predictions [43]. Specifically, the substantial mixing enthalpy prohibits the single-phase stabilization via thermal equilibrium alone [43]. However, this could be compensated by the joint effect of configurational entropy and the reductive environment typically seen in CL-DRM. A significant lattice expansion is observed in the halite phase of HEO catalysts recovered after 3 and 100 CL-DRM cycles (from $a = 4.18\text{--}4.28\text{ \AA}$, see Figure S1 and Table S2), indicating the incorporation of larger Mn^{2+} and Fe^{2+} cations. However, the CL-DRM performance of unsupported HEO is underwhelming (Figure S2), owing to its poor dispersion and a specific surface area that is too low for any meaningful chemical application. To address this issue, the prepared HEO is supported on ZrO_2 , which could effectively increase the surface area and pore volume by up to ca. 3 and 11 folds (Figure S3 and Table S3). The

introduction of ZrO_2 support could also improve the catalyst hardness [52,53], which is an important consideration in practical applications, including chemical looping and conventional catalytic reactors.

Accordingly, we prepared HEO/ ZrO_2 with 30 mol % ZrO_2 (metal basis), as well as a series of medium entropy oxides (MEOs, consisting of 4 of the 5 metal elements in HEO, see Table S1) supported on 30 mol % ZrO_2 . Powder XRD revealed that all supported HEO and MEO samples consist of a mixture of a m- ZrO_2 phase, a spinel phase ($a \sim 8.34\text{ \AA}$), and a halite phase ($a \sim 4.17\text{ \AA}$), except for MEO(-Mg) and MEO(-Ni), which do not contain any halite phase (Fig. 2a). The equimolar compositions of constituent Mg, Co, Ni, Mn, Fe were corroborated independently by ICP-OES and XRF analyses (Tables S4–S7). To further characterize the redox activities of the samples, H_2 -TPR was performed up to $900\text{ }^\circ\text{C}$. In general, the HEO and MEOs exhibited two major reduction peaks at 500 and $600\text{ }^\circ\text{C}$ (Fig. 2b). The $500\text{ }^\circ\text{C}$ H_2 consumption peak was attributed to comparatively active lattice oxygens corresponding to the reduction of Co^{3+} , Ni^{2+} , Mn^{3+} to Mn^{2+} , and Fe^{3+} to Fe^{2+} , typically leading to the full oxidation of hydrocarbons and hence are not desired by CL-DRM. The larger H_2 -TPR peak at $600\text{ }^\circ\text{C}$ suggests the presence of lattice oxygen that is suitable for the partial oxidation of methane to CO and H_2 . Furthermore, the reduction events of the HEO and MEO samples occur at higher temperatures than any of the monometallic oxides (Figure S4). This is ascribed to the entropic stabilization of the HEO and MEO. Lastly, SEM and TEM characterization of the HEO/ ZrO_2 displayed a porous morphology with grain size of ca. 50 nm , forming an intimate mixture of the spinel, halite, and m- ZrO_2 phases at nanoscale (Fig. 2c–f).

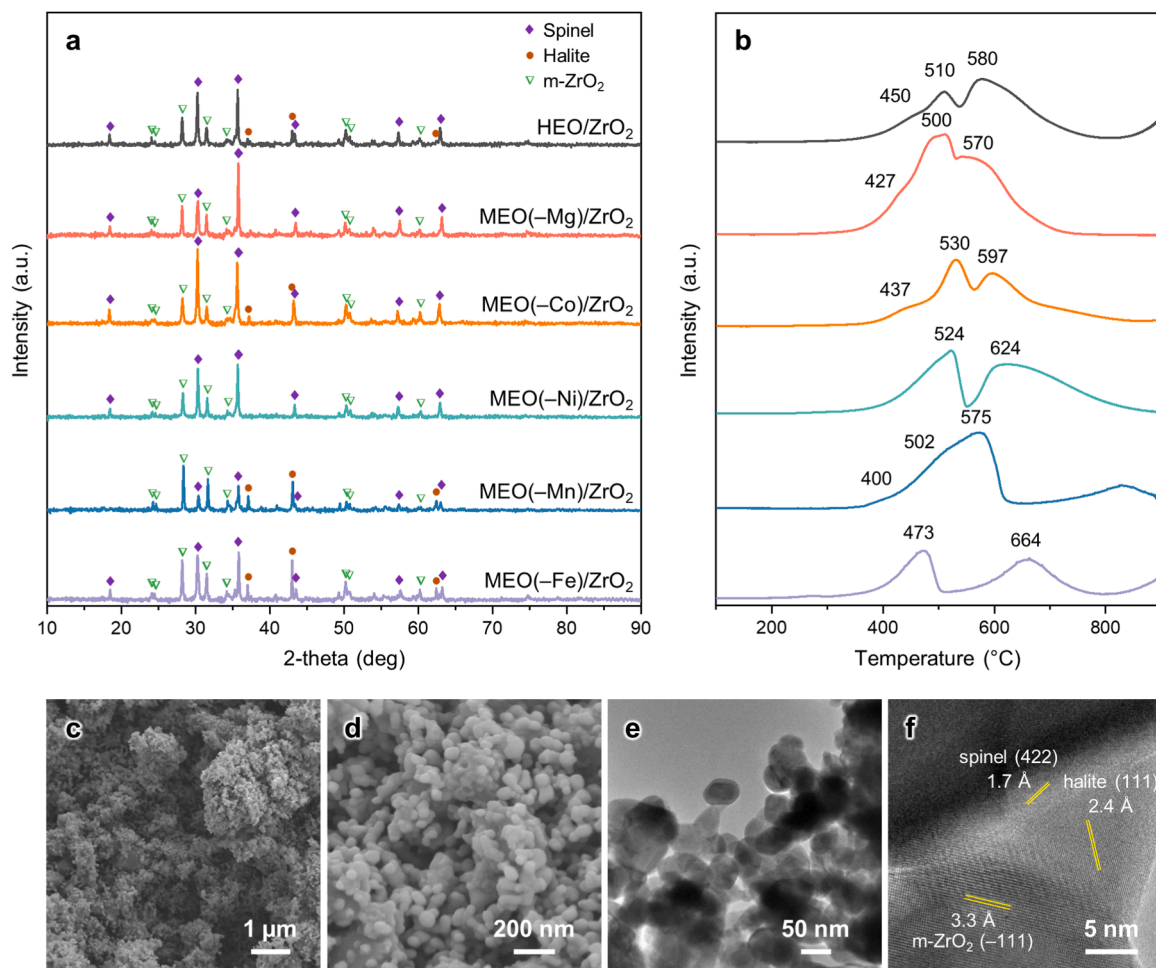


Fig. 2. (a) XRD patterns and (b) H_2 -TPR profiles of HEO/ ZrO_2 and various MEO/ ZrO_2 . (c, d) FESEM images and (e, f) FETEM images of HEO/ ZrO_2 .

3.2. Chemical looping–dry reforming of methane

The catalytic performance of the synthesized HEO/ZrO₂ and MEO/ZrO₂ redox catalysts for CL–DRM was evaluated in a tubular fixed bed reactor, by periodically alternating the inlet gas composition between 5 % CH₄ and 10 % CO₂ (with purge in-between). Amongst all samples, HEO/ZrO₂ showed outstanding CH₄ conversion (43 % by the 100th cycle), syngas selectivity (97 % by the 100th cycle), and cyclic stability, after an induction phase over the initial 10 cycles (Fig. 3a, b). MEO(–Ni)/ZrO₂ showed the lowest CH₄ conversion (around 6 %), probably owing to the lack of Ni, which plays a pivotal role in CH₄ activation. In previous studies, Mg and Mn were regarded as crucial promoters for 3d transition metal HEOs [42]. Indeed, in the absence of Mg or Mn, i.e. MEO(–Mg)/ZrO₂ and MEO(–Mn)/ZrO₂, low apparent CH₄ conversions of 11 % and 30 % were observed, respectively. MEO(–Fe)/ZrO₂ showed the best initial activity, with CH₄ conversion of 73 % at the 3rd cycle, after which the activity drastically declined, with 37 % CH₄ conversion at the 100th cycle. Such deactivation is attributed to coking, as Fe is regarded as a dopant that could effectively suppress coking during conventional DRM [54,55]. Amongst all MEO catalysts, MEO(–Co)/ZrO₂ displayed cyclic stability and the highest cyclic methane conversion (48 % by the 100th cycle). MEO(–Mn)/ZrO₂ and MEO(–Ni)/ZrO₂ afforded the lowest syngas selectivity of 80–85 % while MEO(–Co)/ZrO₂ and MEO(–Fe)/ZrO₂ maintained 100 % syngas selectivity. This suggests that Mn may be an important constituent in tuning the lattice oxygen activity towards methane reforming. Overall, the performance of the MEO(–Co)/ZrO₂ is the most comparable to, and even marginally surpassing the performance of HEO/ZrO₂ over 100 cycles. Here, the slightly higher activity of MEO(–Co)/ZrO₂ than HEO/ZrO₂ may be rationalized by the dilution of Ni sites by Co in HEO/ZrO₂. On the other hand, an earlier study suggests that coke deposition on Ni is ca. 20 times faster than that on Co during DRM [56]. Indeed, the non-oxidative activation of CH₄, i.e. coking, is much severer on MEO

(–Co)/ZrO₂ than on HEO/ZrO₂, as shown by the quantification of CH₄ decomposition in Fig. 3b(inset) and S5. Although CL–DRM could effectively alleviate coke accumulation, it is still desirable to suppress coking and promote methane reforming, which offer the following advantages (i) maintaining activity of the metal active sites and (ii) controlling the H₂:CO ratios of the gases produced during the reforming and the regeneration stages. Indeed, despite the apparent cyclic stability of MEO(–Co)/ZrO₂, which was exposed to 2 min of CH₄ and 5 min CO₂ in each cycle, as shown in Fig. 3a, when the duration of catalyst regeneration (i.e. CO₂ exposure) was reduced from 5 min to 1 min in each cycle, the activity of MEO(–Co)/ZrO₂ underwent an obvious decline, with cyclic CH₄ conversion dropping by 17 % over 100 cycles. In comparison, the performance of HEO/ZrO₂ remained stable under the same conditions (Figure S6a), signifying better coking resistance. Raman spectroscopy of the spent catalysts (i.e. after 100 CL–DRM cycles) depicts intense peaks attributed to carbon deposition on the spent MEO(–Co)/ZrO₂ (Figure S6b) with considerable carbon nanotubes observed by SEM (Figure S7). In comparison, HEO/ZrO₂ suffered from much less coking with lower carbon peak intensities in the Raman spectrum (Figure S6b) and negligible presence of carbon nanotubes in the spent catalysts (Figure S7). From this point of view, HEO/ZrO₂ is deemed a superior redox catalyst over MEO(–Co)/ZrO₂ and all other MEO/ZrO₂ catalysts.

Besides the MEO catalysts, the CL–DRM performance of HEO/ZrO₂ catalyst was also compared against NiFeO_x/Al₂O₃, which has been widely reported as a superior catalysts in conventional steam reforming of methane [57], dry reforming of methane [54], and chemical looping–steam reforming of methane [32]. The CL–DRM performance of HEO/ZrO₂, NiFeO_x/Al₂O₃, and NiFeO_x/ZrO₂ over 100 redox cycles are compared in Fig. 3c–e. NiFeO_x/ZrO₂ displayed the worst performance, with declining cyclic CH₄ conversion from 25 % to 4 % over 100 cycles; its syngas selectivity was only 20–40 %. NiFeO_x/Al₂O₃ initially delivered a high CH₄ conversion of 93 % at the 2nd cycle, followed by rapid deterioration over consecutive cycles. The cyclic CH₄ conversion for

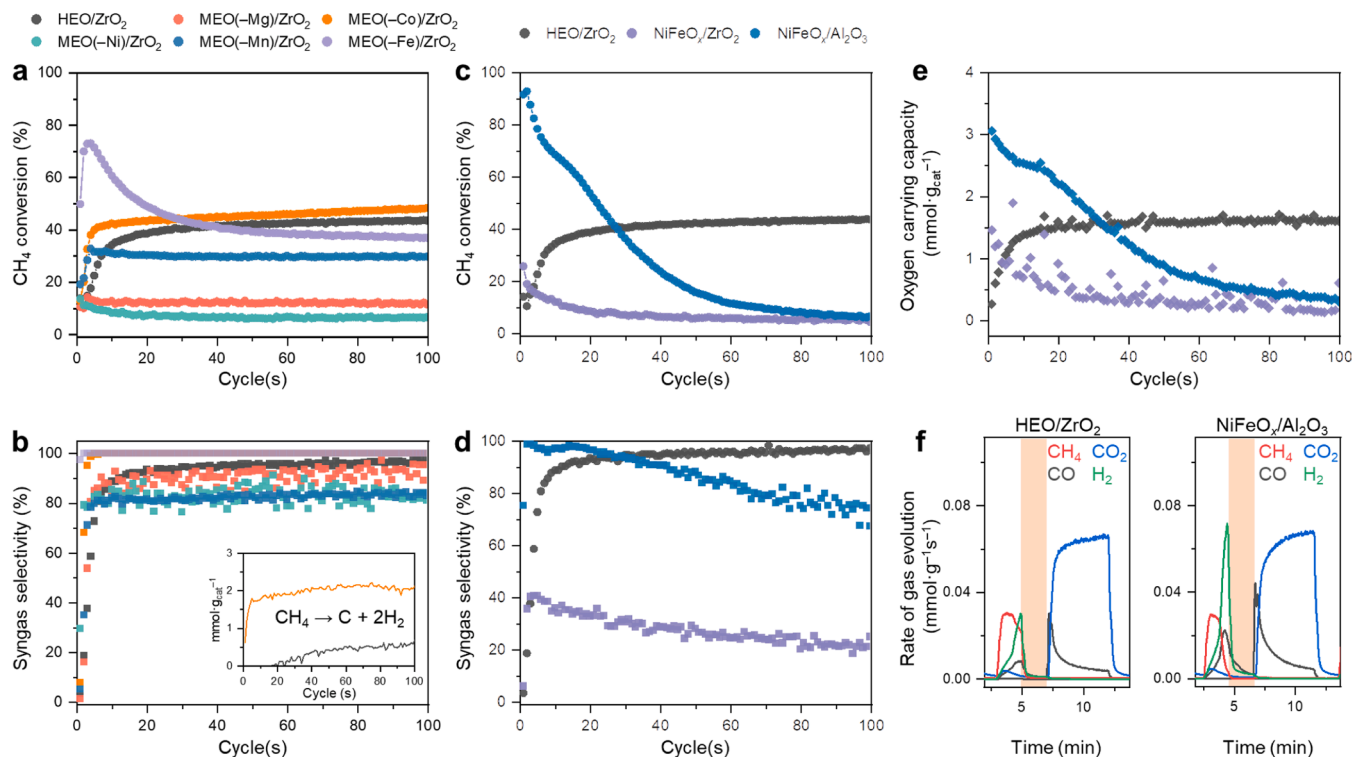


Fig. 3. Catalytic performance for chemical looping dry reforming of methane. (a) Cyclic CH₄ conversion and (b) Syngas selectivity per cycle of HEO/ZrO₂ and various MEO/ZrO₂ catalysts. The inset in (b) shows the amount of CH₄ decomposition per gram of catalyst per cycle for HEO/ZrO₂ and MEO(–Co)/ZrO₂. (c) CH₄ conversion, (d) Syngas selectivity, and (e) oxygen carrying capacity per cycle of HEO/ZrO₂ and the benchmark NiFeO_x catalysts supported on Al₂O₃ or ZrO₂. (f) Gas evolution rate profiles of HEO/ZrO₂ vs. NiFeO_x/Al₂O₃.

NiFeO_x/Al₂O₃ dropped by half in 25 cycles and eventually to 6 % by the 100th cycle (Fig. 3c). The same declines were observed in its syngas selectivity and oxygen carrying capacity (Fig. 3d, e). As illustrated by the profiles of rates of gas evolution during the 6th cycle (Fig. 3f), more CO evolved during the purging stage for NiFeO_x/Al₂O₃, signifying the slow reaction between the deposited carbon and the residual lattice oxygen in the reduced NiFeO_x/Al₂O₃ (Figure S8a). This residual CO evolution is much less profound in the case of HEO/ZrO₂. In other words, the extent of carbon deposition on NiFeO_x/Al₂O₃ is severer than on HEO/ZrO₂. On the other hand, the regeneration stage (i.e. when CO₂ is fed to the reactor) in the CL-DRM cycling experiment was sufficiently long to prevent any accumulation of carbon on these catalysts, as corroborated by the absence of any carbon peak in the Raman spectra for the spent HEO/ZrO₂, NiFeO_x/Al₂O₃, and NiFeO_x/ZrO₂ (Figure S8b, c). At the same time, SEM images of the spent catalysts revealed severe sintering for NiFeO_x/Al₂O₃ and NiFeO_x/ZrO₂ (Figures S9 and S10). Therefore, sintering is deemed the primary cause of catalyst deactivation for the two NiFeO_x based catalysts. To conclude, the HEO/ZrO₂ catalyst exhibited far superior performance in terms of catalytic activity,

stability, syngas selectivity, and cyclic oxygen carrying capacity than the NiFeO_x benchmarks throughout the 100 CL-DRM cycles.

3.3. Evolution of HEO catalysts over CL-DRM cycles

An induction period approximately spanning over the first 15–20 cycles was observed for the HEO/ZrO₂ catalyst (Fig. 3a, b). The rapidly ascending CH₄ conversion and syngas selectivity over the first few cycles was attributed to catalyst activation (exsolution of metallic nanoparticles) and phase transformation from a mixed spinel-halite composite to a single halite-phase HEO. As a result, the catalytic activity towards CH₄ is significantly enhanced, accompanied by the increased extent of catalytic CH₄ decomposition during the reforming stage. By the 15th cycle, methane decomposition has become a significant contributor to methane activation, as shown in the inset of Fig. 3b inset).

The evolution of the phase composition of the (MgCoNiMnFe)O_x/ZrO₂ catalyst sample was characterized by XRD when it was freshly prepared, after 3 CL-DRM cycles and after 100 CL-DRM cycles, as shown in Fig. 4a, b. The freshly calcined HEO/ZrO₂ (denoted as HEO/

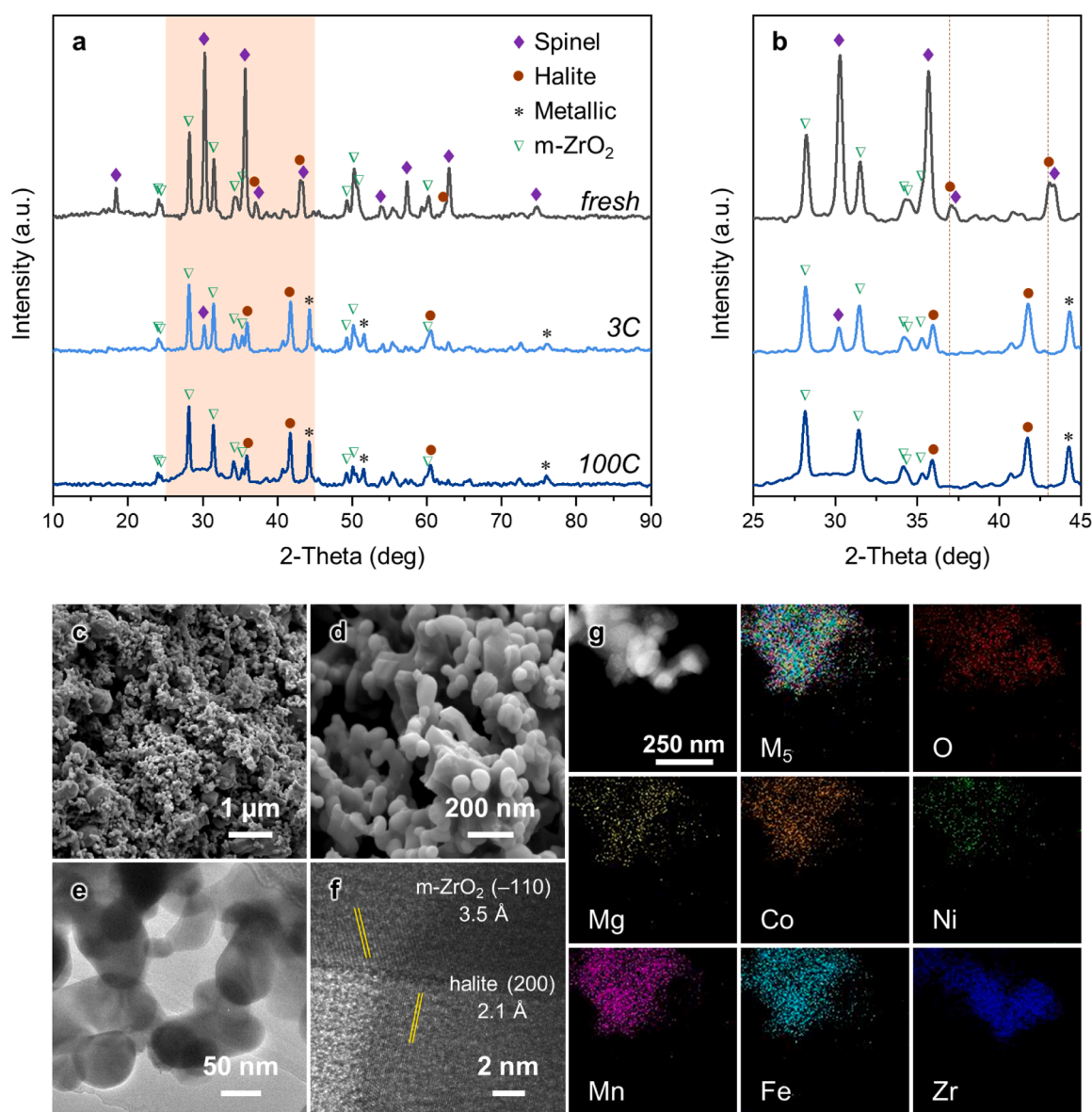


Fig. 4. (a) Full-range and (b) focused XRD profiles of HEO/ZrO₂-fresh (as prepared), 3 C (recovered after the 3rd CO₂ treatment), and 100 C (after the 100th CO₂ treatment). (c, d) FESEM images, (e, f) FETEM images, and (g) EDX elemental mappings of the recovered HEO/ZrO₂-100 C (oxidized form) after 100 CL-DRM cycles.

ZrO₂-fresh) consists of three phases: m-ZrO₂, spinel, and halite. After 100 cycles in its oxidized state, i.e., HEO/ZrO₂-100 C, the spinel phase in the catalyst completely disappeared, leaving a mixture of m-ZrO₂, halite, and a metal with face centered cubic (fcc) structure (Fig. 4a). The halite diffraction peaks shift slightly towards lower 2 θ , suggesting lattice expansion (from $a = 4.17\text{--}4.33\text{ \AA}$, Fig. 4b); this is attributed to the incorporation of the large Mn²⁺ and Fe²⁺ cations into the halite structure, which originally consisted of Co²⁺, Ni²⁺, Mg²⁺. An intermediate state is observed in the HEO/ZrO₂ catalyst recovered after the 3rd cycle (HEO/ZrO₂-3 C), showing a small amount of spinel alongside the m-ZrO₂, halite, and fcc metal (Fig. 4b). Although the spinel phase has mostly diminished by the 3rd cycle, the structure and phase composition of the HEO/ZrO₂ catalyst could continue to evolve at length scales undetectable by the lab XRD. Rietveld refinement of the XRD patterns revealed more details of the phase evolution, as shown in Figure S11 and Table S8.

In addition, the spent MEO/ZrO₂ catalysts are found to consist of m-ZrO₂, halite, and/or metallic phases (Figure S12a), whereas the spent NiFeO_x/Al₂O₃ displays a mixture of metal and FeAl₂O₄ (Figure S12b); the latter is known for its low redox activities [58,59]. The spent NiFeO_x/ZrO₂ exhibits a phase composition consisting of metal, spinel and m-ZrO₂ (Figure S12b). While ZrO₂ could stabilize NiFe-spinels from thermal-sintering in inert conditions, it may be inadequate in preventing phase segregation-induced sintering, which are typically observed during chemical looping processes [60]. In contrast, the high entropy effect could effectively mitigate the adverse effects associated with cyclic phase changes, such as irreversible phase segregation and sintering [42]. In addition to XRD analysis, the compositional evolution of the catalysts over CL-DRM cycles was substantiated by Raman spectroscopy (Figure S13), in which the m-ZrO₂ phase contributes the majority of Raman scattering signals [61]. In comparison, the fresh catalysts show bands originating from the spinel phase [62], which decreased after 3

cycles and completely disappeared after 100 cycles.

Fig. 4c–f depicts the SEM and TEM images of HEO/ZrO₂-100C. From the observed morphology, minimal sintering took place over the 100 CL-DRM cycles, with the spent catalyst presents a similar porous morphology as the fresh catalyst with grain size of ca. 50 nm. High resolution TEM analysis reveals that the cycled catalyst largely consists of halite (HEO) mixed with m-ZrO₂ (Fig. 4f). The EDX elemental maps (Fig. 4g) show a uniform spatial distribution of Mg, Co, Ni, Mn, and Fe at the upper-left region; this is especially obvious in the superimposed elemental maps (labeled M₅). These elemental maps support the presence of a HEO with five metal constituents. Meantime, Zr could be observed at regions where the signals of the 3d metals and Mg are relatively weak, signifying the role of ZrO₂ as a support material for the active HEO.

The catalytic and redox behaviors of HEO/ZrO₂ after 100 CL-DRM cycles was further investigated by subjecting it to one more period of CH₄ reforming at 800 °C, denoted as HEO/ZrO₂-101 M. Based on the XRD results (Fig. 5a), HEO/ZrO₂-101M consists of the same three phases (m-ZrO₂, halite, and fcc metal), but with a notable amount of the halite phase reduced to the metallic phase (Table S8). Accordingly, the SEM and TEM images (Fig. 5c–f) show that the HEO/ZrO₂-101M sample is dominated by the presence of metal nanoparticles, in which Ni, Co and Fe were the major metal element (Fig. 5g) that exsolved from the halite HEO matrix. At the same time, the reduced catalyst shows the same porous morphology as the oxidized catalyst and the fresh one (Fig. 5c–d), signifying the excellent sintering resistance. Interestingly, after reduction the halite phase still appear to be a solid solution of Mg, Co, Ni, Mn, Fe, and O, supported on ZrO₂. The residual Ni²⁺, Fe²⁺ and Co²⁺ cations suggest the inherent thermodynamic stability of the halite solid solution; this is in line with the findings of previous studies [63].

The chemical states and local environments of the redox-active species and their participation during CL-DRM were further

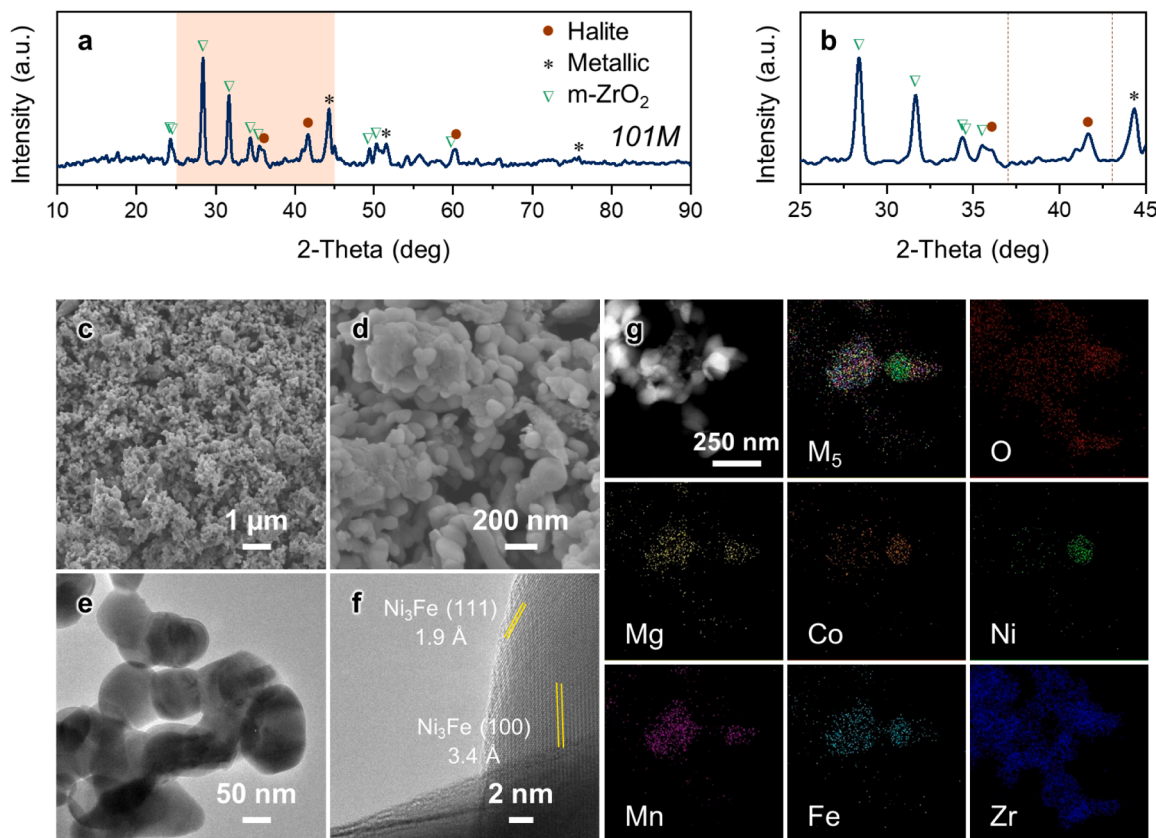


Fig. 5. (a) Full-range and (b) focused XRD profiles of HEO/ZrO₂-101 M (after the 101st CH₄ exposure). (c, d) FESEM images, (e, f) FETEM images, and (g) EDX elemental mappings of the recovered HEO/ZrO₂-101M (reduced form) after 100 CL-DRM cycles.

characterized by XAFS and XPS, to probe the reaction model at an atomic scale. XAFS was conducted for the K edges of Co, Ni, Mn, and Fe in HEO/ZrO₂-100C and HEO/ZrO₂-101M in transmission mode. Here, the 100C and 101M states corresponds to the oxidized (by CO₂) and reduced (by CH₄) states, respectively, when the HEO catalyst has reached compositional equilibrium during CL-DRM. The measured spectra were calibrated and compared against standards, including metal foils and various oxides. Linear combination fittings (LCF) were conducted for the XANES spectra (Figure S14 and Table S9). Fittings of the FT-EXAFS data were performed for three most relevant shells: the first metal-metal shell M-M(m) of the alloys (space group Fm-3 m), the first metal-oxygen shell M-O(o) and the first metal-metal shell M-M(o) of the halite-phase oxides (Fm-3 m), where the symbol m and o in the parentheses corresponds to coordination in the metal phase and the halite phase, respectively. For simplicity, any M_A-M shell (M = Mg, Co, Ni, Mn, Fe) is approximated by the M_A-M_A shell, due their similar atomic numbers and the spatial randomness of the distribution. It is expected that certain metallic species in our catalysts will have smaller apparent average coordination numbers (CNs) than the bulk standards for three reasons: (a) the examined metal may present in more than one phases, hence their distribution leads to lower CNs [64]; (b) small metal clusters usually exhibit lower CNs owing to the high proportion of low

coordination surface atoms [65]; and (c) metals having a preferential occupancy of the surface sites in the alloy may also display smaller CNs owing to undercoordination.

The Co K-edge XANES spectra show a close match between Co in HEO/ZrO₂-101M and Co foil (Fig. 6a), suggesting that Co is mostly reduced to metal during the methane reforming stage. The HEO/ZrO₂-100C sample presents a Co valence state between metallic Co and Co₃O₄, with a clear white line feature located at 7724 eV to the left of the white line of Co₃O₄, suggesting an oxidation state similar to CoO. The Co R-space EXAFS spectrum of HEO/ZrO₂-101M displays a univocal Co-M(m) shell, while that of HEO/ZrO₂-100C suggests a combination of Co-M(m), Co-O(o), and Co-M(o) shells. Table S10 shows the fitted structural parameters (based on the FT-EXAFS spectra) of the Co species in HEO/ZrO₂-101M and HEO/ZrO₂-100C. The Co-M(m) shells in HEO/ZrO₂-100C and HEO/ZrO₂-101M exhibits smaller apparent CNs than Co foil, suggesting undercoordinated Co atoms in the alloy. Meanwhile, CNs for Co-O(o) and Co-M(o) shells of the halite phase are close to their standard values of 6 and 12, respectively (Table S10). These fitted coordination numbers corroborate the catalyst structures depicted in Fig. 1, i.e. metal nanoalloys deposited on bulk halite structured HEO matrix.

Wavelet transform of EXAFS (WT-EXAFS) was performed to provide

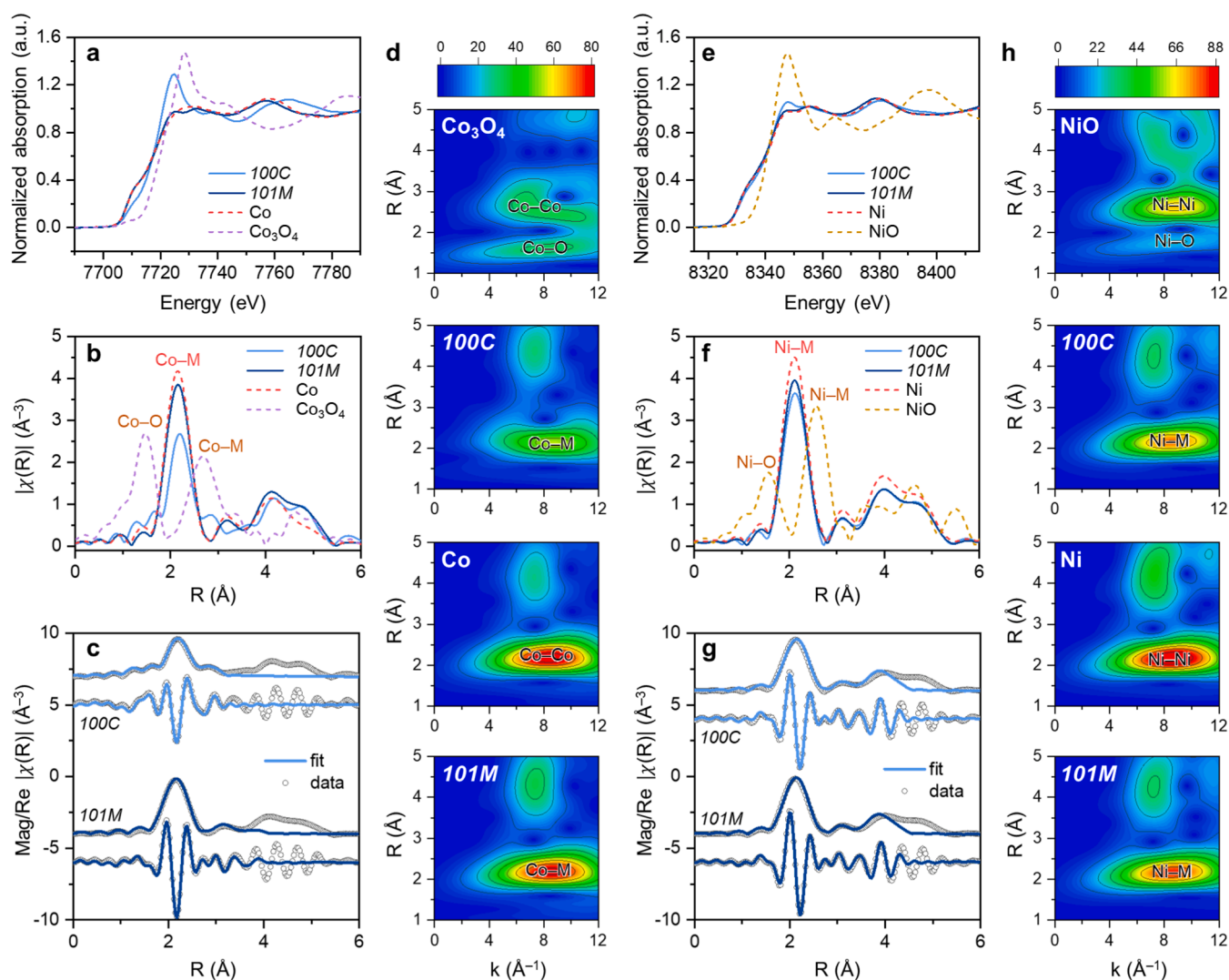


Fig. 6. XAFS studies of Co and Ni in HEO/ZrO₂-100C and 101M: (a) Co K-edge XANES spectra; (b) Co R-space FT-EXAFS spectra; (c) Co EXAFS fittings; (d) Co WT-EXAFS spectra; (e) Ni K-edge XANES spectra; (f) Ni R-space FT-EXAFS spectra; (g) Ni EXAFS fittings; and (h) Ni WT-EXAFS spectra. The EXAFS spectra are k²-weighted.

an intuitive 3D view of the local environment of interested element, correlating the EXAFS spectra in both R-space (phase shift not corrected, a difference up to 0.4 Å is expected) and k-space. In general, higher intensity of the lobe modulus is related to higher EXAFS amplitude; an intense lobe appearing at higher k-space should be related to an element with higher atomic number [66]. For the HEO catalyst, the transition metals are of similar atomic numbers except for Mg which is entirely present in the halite phase. In addition, distortion of the crystal array (e.g., doping) and site vacancies may also lead to lower lobe intensity [67, 68]. The WT-EXAFS spectra of Co foil, Co_3O_4 , HEO/ ZrO_2 -100 C and HEO/ ZrO_2 -101 M are shown in Fig. 6d. It is conspicuous that the Co WT-EXAFS of HEO/ ZrO_2 -101 M and WT-EXAFS of 100 C resemble that of Co metal, with appreciably lower intensity for the Co-M lobe in HEO/ ZrO_2 -100 C because of the mixed metal and oxide composition (vide supra).

The interpretation of Ni K-edge XANES spectra is more straightforward, as both HEO/ ZrO_2 -100C and HEO/ ZrO_2 -101M manifest curves that align well with Ni metal (Fig. 6e). A subtle white line feature is found at 8348 eV for HEO/ ZrO_2 -100C, indicating the presence of some NiO. Accordingly, LCF for the Ni XANES estimated the presence of ca. 14 % of NiO in HEO/ ZrO_2 -100C (Figure S14 and Table S9). Fitting of the Ni-M(m) shells of the FT-EXAFS spectra (Fig. 6f) gives $R = 2.50 \text{ Å}$

and CNs of 10.3 and 11.4, for HEO/ ZrO_2 -100C and HEO/ ZrO_2 -101M, respectively. These values are similar to typical Ni alloys (Fig. 6g and Table S10). Ni WT-EXAFS of Ni metal, HEO/ ZrO_2 -100C, and HEO/ ZrO_2 -101M all display a single lobe located around $R = 2.1 \text{ Å}$, with diminishing intensity according to Ni foil > HEO/ ZrO_2 -101M > HEO/ ZrO_2 -100 C (Fig. 6h).

Mn K-edge XANES spectra for both HEO/ ZrO_2 -100C and HEO/ ZrO_2 -101M lie between the reference spectra of MnO and Mn_2O_3 , with HEO/ ZrO_2 -100C having marginally higher valence (Fig. 7a) than HEO/ ZrO_2 -101M. This suggests that the oxidation state of Mn in the halite HEO is between 2+ and 3+, with Mn being slightly more oxidized after reaction with CO_2 than after methane reforming. Clear white line features are observed for both samples at 6553 eV. The effective bond lengths of Mn-O(o) and Mn-M(o) in HEO/ ZrO_2 -100C and HEO/ ZrO_2 -101M (2.16 Å and 3.08–3.10 Å, respectively) are notably shorter than those in the MnO standard (2.22 Å and 3.14 Å, respectively), see Fig. 7b, c and Table S10), suggesting that MnO is present in a halite solid solution, neighboring considerable amount of metal cations with radius smaller than that of Mn^{2+} .

Based on the Fe K-edge XANES spectra (Fig. 7e), the oxidation state of Fe species in the HEO catalyst swings between FeO and Fe over a CH_4 - CO_2 redox cycle. A white line feature at 7127 eV is present in both

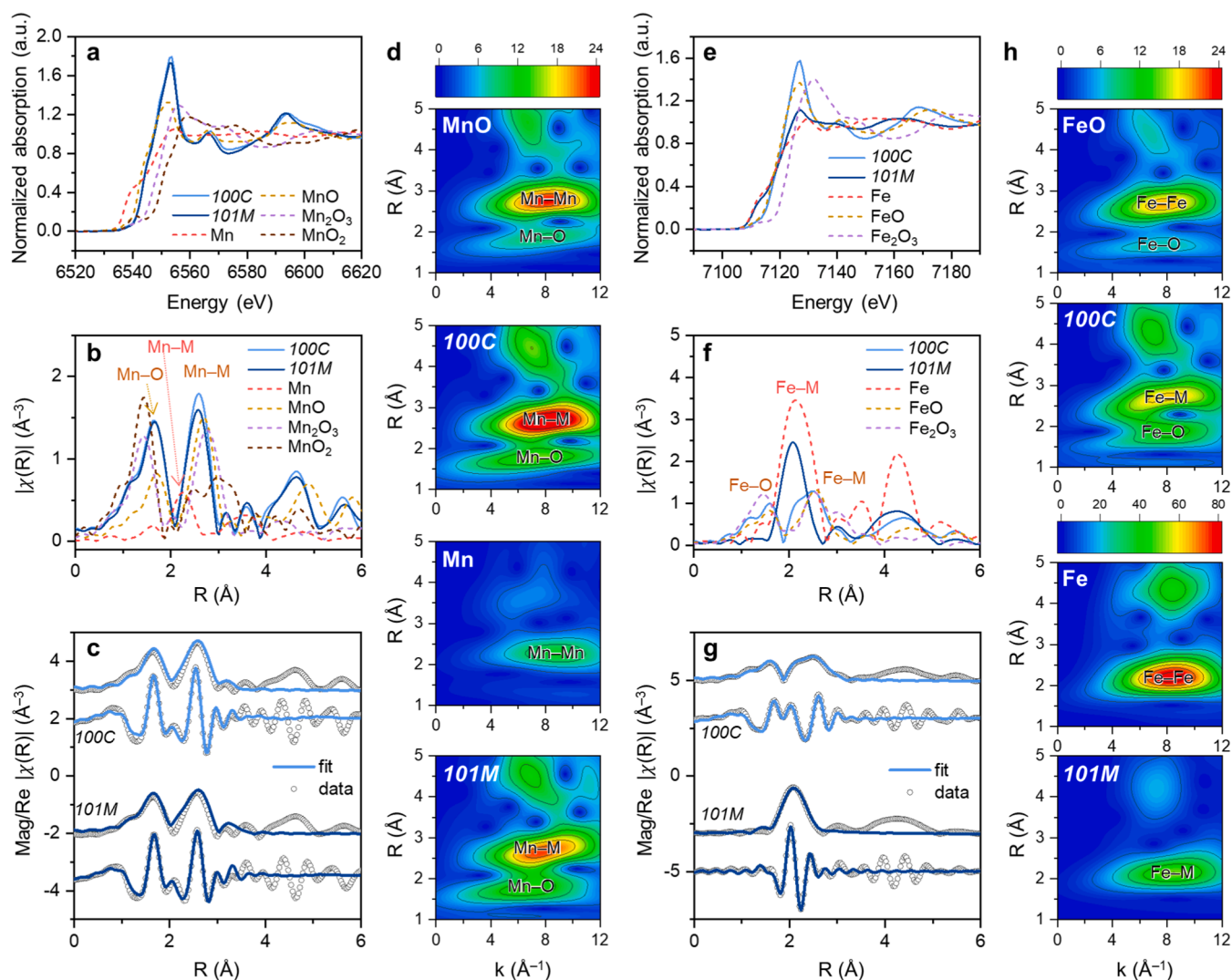


Fig. 7. XAFS studies of Mn and Fe in HEO/ ZrO_2 -100 C and 101 M: (a) Mn K-edge XANES spectra; (b) Mn R-space FT-EXAFS spectra; (c) Mn EXAFS fittings; (d) Mn WT-EXAFS spectra; (e) Fe K-edge XANES spectra; (f) Fe R-space FT-EXAFS spectra; (g) Fe EXAFS fittings; and (d) Fe WT-EXAFS spectra. The EXAFS spectra are k^2 -weighted.

samples, indicating the presence of FeO in both redox stages. LCF of the XANES spectra estimates 32 % FeO and 68 % Fe in HEO/ZrO₂-101M, and 100 % FeO in HEO/ZrO₂-100C (Figure S14 and Table S9). The fitted Fe-O(o) and Fe-M(o) distances in HEO/ZrO₂-100C, based on FT-EXAFS, also show lattice contraction relative to the reference FeO (Table S10), suggesting the neighborhood of smaller cations in the halite solid solution. HEO/ZrO₂-101M exhibits a rather low apparent CN of 5.0 for Fe-M(m) shell (Table S10) as well as a low-intensity Fe-M lobe in WT-EXAFS (Fig. 7h), indicating an undercoordinated environment of Fe atoms in the alloy. This may be attributed to (i) Fe being concentrated at the surface of the nanoalloy particles, (ii) the nanoalloy particles are small in size [65], or (iii) both.

The chemical states in the surface regions of the redox catalyst in its various stages of CL-DRM cycles are characterized by XPS, as shown in Fig. 8. The oxidation states beneath the surface layer were also probed

by XPS measurements after argon plasma cleaning. In the *fresh* catalyst, Co, Mn, and Fe are presented in both 2+ and 3+ valence states, as they exist in spinel and halite phases. After 3 cycles (after CO₂-oxidation), similar chemicals states were identified as in the *fresh* catalyst, with mixed 2+ and 3+ valence states for Co, Mn, and Fe. After Ar-cleaning, the Co, Mn, and Fe species show increased proportions of 2+ valence states owing to the lack of oxidation beneath the surface region. A small fraction of metallic Ni was identified in the Ar-cleaned HEO/ZrO₂-3C. After 100 cycles of CL-DRM reaction, some metallic Co is identified in the Ar-cleaned HEO/ZrO₂-100C catalyst, while more Ni is found in metallic state, accompanied by dwindling signals of the NiO doublet at ca. 854 eV (HEO/ZrO₂-*fresh* > HEO/ZrO₂-3C > HEO/ZrO₂-100C, Fig. 8b). The peak at 854 eV is attributed to a non-local screening effect of adjacent Ni²⁺ [69,70], therefore, as the HEO progressively form over CL-DRM cycles, the Ni²⁺ cations in the halite solid solution are

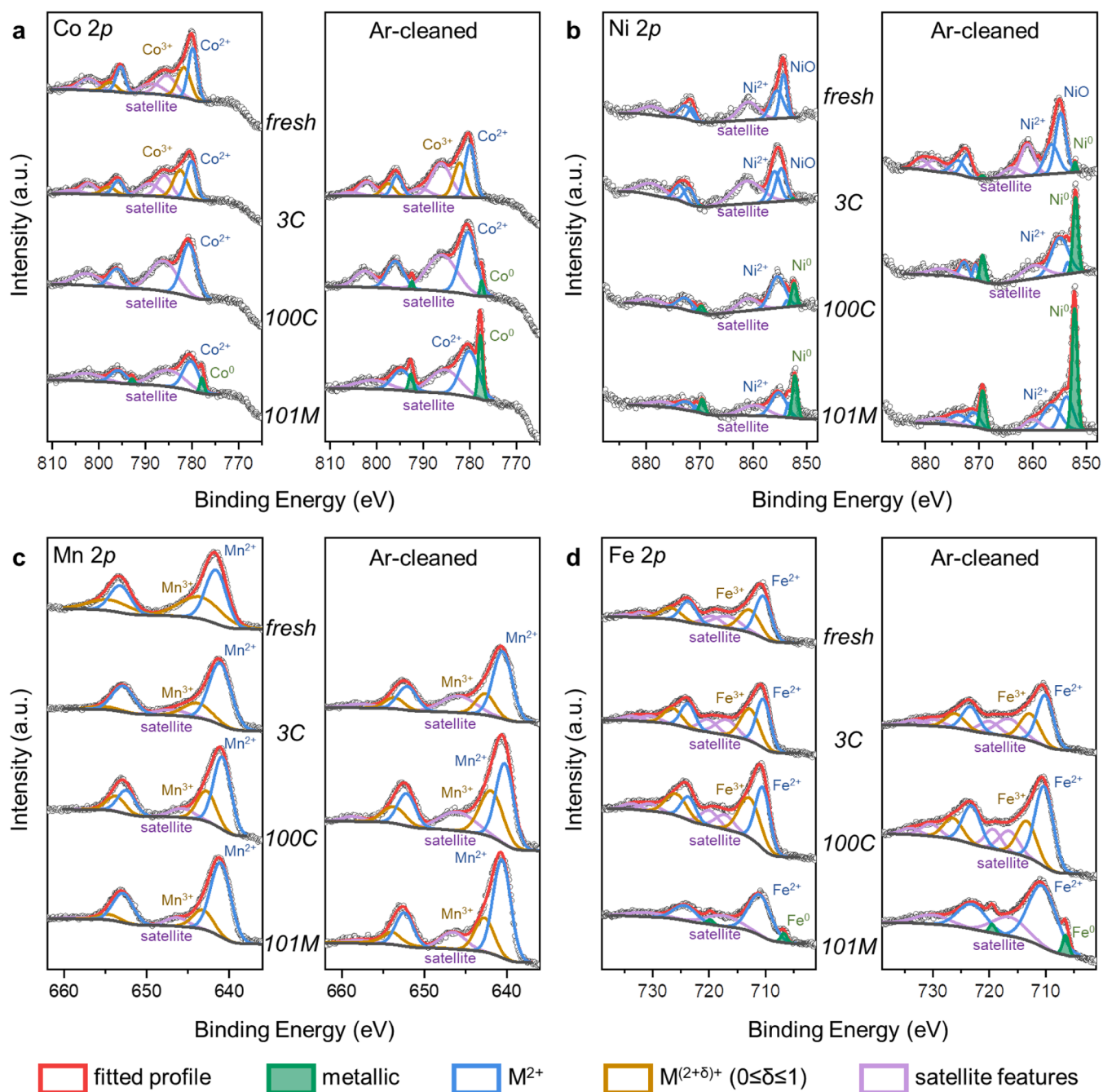


Fig. 8. XPS profiles and deconvolutions for (a) Co 2p, (b) Ni 2p, (c) Mn 2p, and (d) Fe 2p regions of HEO/ZrO₂-*fresh*, 3C, 100C, and 101M.

neighbored by increasingly fewer Ni^{2+} cations. The XPS peak at ca. 856 eV corresponds to Ni^{2+} that is typically seen in $\text{Ni}(\text{OH})_2$. Mn and Fe are present in 2+ and 3+ states in the oxidized catalyst. In the reduced HEO/ZrO_2 -101 M catalyst, metallic Fe, and Mn-oxides are formed, with the surface appearing more oxidized than sub-surface (*i.e.* after Ar-cleaning). It should be noted that the XPS results generally show higher oxidation states of Co, Ni, Mn, and Fe in the spent HEO/ZrO_2 samples than the XAFS results. This difference is attributed to the surface oxidation of the samples when they are exposed to air during sample preparation. Given that XPS is a surface-sensitive technique whereas XAFS is a bulk technique, the former is more sensitive to surface oxidation in air. To verify this hypothesis, we performed additional XPS measurements of the spent catalysts after Ar-cleaning and observed significantly lower oxidation states for Co, Ni, Mn, and Fe, as shown in Figure S15. Additional XPS results and analyses are presented in Figure S16, evidencing that the chemical states of Mg and Zr are unchanged throughout the process, in the form of Mg^{2+} (MgO) and Zr^{4+} (m-ZrO_2), respectively.

Based on the comprehensive experimental evidence above, the following reaction model can be established: after the HEO catalyst has reached its equilibrium composition, CH_4 is partially oxidized by the lattice oxygen from the halite structured HEO, resulting in the exsolution of nanoalloys containing primarily Ni, Co, and Fe. During CH_4 reforming, the alloy acts as active site for C–H cleavage, while the release of lattice oxygen associated with the exsolution process is responsible for both oxidative CH_4 activation and coke removal. Upon oxidation by CO_2 (regeneration), most of the metallic Fe and Co, with a fraction of Ni in the alloy are transformed back into 2+ states and redissolved back into the halite HEO. In the meantime, MgO and m-ZrO_2 refrained from participating in the redox cycles and functioned as structural promoters, to facilitate the exsolution-redissolution of metal species and to maintain the active phase dispersion, respectively. The high entropy effect contributes to the stabilization of the halite structure of HEO after a large amount of oxygen released, whilst facilitating cyclic exsolution of nanoalloys as a means of regulating the sizes of the nanoparticles and alleviating sintering [42]. Additionally, the entropy effect drives the cyclic regeneration of a homogeneous halite phase, prevent phase segregation that is otherwise common in chemical looping applications. As a result, we postulate the roles of the individual components in the equilibrated $(\text{MgCoNiMnFe})\text{O}_x$ HEO/ZrO_2 catalyst as follows: (i) MgO_x and MnO_x mainly acted as structural stabilizers that maintained the halite matrix over redox cycles; (ii) the exsolution of Fe, Co, and Ni species supplied appropriately active lattice oxygen for methane reforming; (iii) the exsolved NiFeCo nanoalloys functioned as the active site for methane reforming with attenuated coke formation; (iv) all metal species contributed to the entropy effect that stabilized and anchored the nanoalloys, while providing an entropy-stabilized sink for the recovery of metal cations during catalyst regeneration; and (v) m-ZrO_2 served as an excellent support material which facilitates and maintains the dispersion of HEO active phase, affording decent apparent activity and cyclic durability.

4. Conclusion

In summary, a halite structured $(\text{MgCoNiMnFe})\text{O}_x$ high entropy oxide was designed and synthesized through co-precipitation, calcination and *in situ* transformation over CL–DRM cycles. Compared to a $\text{NiFeO}_x/\text{Al}_2\text{O}_3$ benchmark and MEO/ZrO_2 counterparts, the HEO/ZrO_2 catalyst achieved outstanding performance in terms of high CH_4 conversion per cycle, 97 % selectivity toward syngas, and excellent cyclic stability over 100 CL–DRM cycles. The high entropy effect plays a crucial role in this process, as it facilitates the rapid and reversible exsolution–dissolution cycles of metallic Ni, Fe and Co species, enabling (i) oxygen exchange over the reforming-regeneration cycles, (ii) stabilization of exsolved NiFeCo nanoalloys against sintering, enabling efficient C–H activation; and (iii) cyclic recovery of oxidized Ni, Fe and Co

cations back into HEO matrix, thereby reducing the tendency for sintering and particle aggregation. When supported on 30 mol % ZrO_2 , the HEO/ZrO_2 is able to preserve its phase composition and porous morphology over CL–DRM cycles at 800 °C. By showcasing the unique advantages of high entropy oxides for catalyzing CL–DRM, this work suggests potentials in exploiting high entropy materials in a wide range of chemical looping applications. Future research in the area of HEO-catalyzed CL–DRM should focus more efforts in optimizing the catalyst composition, the HEO constituents, and the operating conditions of the CL–DRM process to further improve process efficiency and stability.

CRedit authorship contribution statement

Syed Saqline: Data curation. **Wen Liu:** Writing – review & editing, Supervision, Resources, Conceptualization. **Preston Tan:** Data curation. **Xianyu Wu:** Data curation. **Chao Wu:** Data curation. **Shibo Xi:** Data curation. **Yu Shao:** Writing – review & editing, Writing – original draft, Formal analysis, Data curation, Conceptualization.

Declaration of Competing Interest

The authors declare that they have no known competing financial interests or personal relationships that could have appeared to influence the work reported in this paper.

Data Availability

Data will be made available on request.

Acknowledgements

This research is funded by the National Research Foundation (NRF), Prime Minister's Office, Singapore under its Campus for Research Excellence and Technological Enterprise (CREATE) programme.

Appendix A. Supporting information

Supplementary data associated with this article can be found in the online version at doi:10.1016/j.apcatb.2024.124191.

References

- [1] Y. Yao, Q. Dong, A. Brozena, J. Luo, J. Miao, M. Chi, C. Wang, I.G. Kevrekidis, Z. J. Ren, J. Greeley, G. Wang, A. Anapolsky, L. Hu, High-entropy nanoparticles: synthesis-structure-property relationships and data-driven discovery, *Science* 376 (2022) eabn3103, <https://doi.org/10.1126/science.eabn3103>.
- [2] Y. Sun, S. Dai, High-entropy materials for catalysis: a new frontier, *Sci. Adv.* 7 (2021) eabg1600, <https://doi.org/10.1126/sciadv.abg1600>.
- [3] C. Oses, C. Toher, S. Curtarolo, High-entropy ceramics, *Nat. Rev. Mater.* 5 (2020) 295–309, <https://doi.org/10.1038/s41578-019-0170-8>.
- [4] J.W. Yeh, S.K. Chen, S.J. Lin, J.Y. Gan, T.S. Chin, T.T. Shun, C.H. Tsau, S.Y. Chang, Nanostructured high-entropy alloys with multiple principal elements: Novel alloy design concepts and outcomes, *Adv. Eng. Mater.* 6 (2004) 299–303, <https://doi.org/10.1002/adem.200300567>.
- [5] B. Cantor, I.T.H. Chang, P. Knight, A.J.B. Vincent, Microstructural development in equiatomic multicomponent alloys, *Mater. Sci. Eng. A* 375 (2004) 213–218, <https://doi.org/10.1016/j.msea.2003.10.257>.
- [6] Y. Yao, Z. Huang, P. Xie, S.D. Lacey, R.J. Jacob, H. Xie, F. Chen, A. Nie, T. Pu, M. Rehwaldt, D. Yu, M.R. Zachariah, C. Wang, R. Shahbazian-Yassar, J. Li, L. Hu, Carbothermal shock synthesis of high-entropy-alloy nanoparticles, *Science* 359 (2018) 1489–1494, <https://doi.org/10.1126/science.aan5412>.
- [7] P. Xie, Y. Yao, Z. Huang, Z. Liu, J. Zhang, T. Li, G. Wang, R. Shahbazian-Yassar, L. Hu, C. Wang, Highly efficient decomposition of ammonia using high-entropy alloy catalysts, *Nat. Commun.* 10 (2019) 4011, <https://doi.org/10.1038/s41467-019-11848-9>.
- [8] X. Qian, D. Han, L. Zheng, J. Chen, M. Tyagi, Q. Li, F. Du, S. Zheng, X. Huang, S. Zhang, J. Shi, H. Huang, X. Shi, J. Chen, H. Qin, J. Bernholc, X. Chen, L.Q. Chen, L. Hong, Q.M. Zhang, High-entropy polymer produces a giant electrocaloric effect at low fields, *Nature* 600 (2021) 664–669, <https://doi.org/10.1038/s41586-021-04189-5>.
- [9] C.M. Rost, E. Sachet, T. Borman, A. Moballeghe, E.C. Dickey, D. Hou, J.L. Jones, S. Curtarolo, J.P. Maria, Entropy-stabilized oxides, *Nat. Commun.* 6 (2015) 8485, <https://doi.org/10.1038/ncomms9485>.

- [10] J. Dąbrowa, M. Stygar, A. Mikula, A. Knapik, K. Mroczka, W. Tejchman, M. Danielewski, M. Martin, Synthesis and microstructure of the (Co,Cr,Fe,Mn,Ni)₃O₄ high entropy oxide characterized by spinel structure, *Mater. Lett.* 216 (2018) 32–36, <https://doi.org/10.1016/j.matlet.2017.12.148>.
- [11] J. Gild, Y. Zhang, T. Harrington, S. Jiang, T. Hu, M.C. Quinn, W.M. Mellor, N. Zhou, K. Vecchio, J. Luo, High-entropy metal diborides: a new class of high-entropy materials and a new type of ultrahigh temperature ceramics, *Sci. Rep.* 6 (2016) 37946, <https://doi.org/10.1038/srep37946>.
- [12] P. Sarker, T. Harrington, C. Toher, C. Oses, M. Samiee, J.P. Maria, D.W. Brenner, K. S. Vecchio, S. Curtarolo, High-entropy high-hardness metal carbides discovered by entropy descriptors, *Nat. Commun.* 9 (2018) 4980, <https://doi.org/10.1038/s41467-018-07160-7>.
- [13] T. Jin, X. Sang, R.R. Unocic, R.T. Kinch, X. Liu, J. Hu, H. Liu, S. Dai, Mechanochemical-assisted synthesis of high-entropy metal nitride via a soft urea strategy, *Adv. Mater.* 30 (2018) e1707512, <https://doi.org/10.1002/adma.201707512>.
- [14] M. Cui, C. Yang, B. Li, Q. Dong, M. Wu, S. Hwang, H. Xie, X. Wang, G. Wang, L. Hu, High-entropy metal sulfide nanoparticles promise high-performance oxygen evolution reaction, *Adv. Energy Mater.* 11 (2020) 2002887, <https://doi.org/10.1002/aenm.202002887>.
- [15] Y. Ma, Y. Ma, S.L. Dreyer, Q. Wang, K. Wang, D. Goonetilleke, A. Omar, D. Mikhailova, H. Hahn, B. Breitung, T. Brezesinski, High-entropy metal-organic frameworks for highly reversible sodium storage, *Adv. Mater.* 33 (2021) e2101342, <https://doi.org/10.1002/adma.202101342>.
- [16] L. Zhang, W. Cai, N. Bao, Top-level design strategy to construct an advanced high-entropy Co-Cu-Fe-Mo (Oxy) hydroxide electrocatalyst for the oxygen evolution reaction, *Adv. Mater.* 33 (2021) e2100745, <https://doi.org/10.1002/adma.202100745>.
- [17] J. Cavin, A. Ahmadiparidari, L. Majidi, A.S. Thind, S.N. Misal, A. Prajapati, Z. Hemmat, S. Rastegar, A. Beukelman, M.R. Singh, K.A. Unocic, A. Salehi-Khojin, R. Mishra, 2D High-entropy transition metal dichalcogenides for carbon dioxide electrocatalysis, *Adv. Mater.* 33 (2021) e2100347, <https://doi.org/10.1002/adma.202100347>.
- [18] Y. Chen, Z.W. Dai, J.Z. Jiang, High entropy metallic glasses: glass formation, crystallization and properties, *J. Alloy. Compd.* 866 (2021) 158852, <https://doi.org/10.1016/j.jallcom.2021.158852>.
- [19] M.D. Alcalá, C. Real, I. Fombella, I. Trigo, J.M. Córdoba, Effects of milling time, sintering temperature, Al content on the chemical nature, microhardness and microstructure of mechanochemically synthesized FeCoNiCrMn high entropy alloy, *J. Alloy. Compd.* 749 (2018) 834–843, <https://doi.org/10.1016/j.jallcom.2018.03.358>.
- [20] V. Soare, M. Burada, I. Constantin, D. Mitrica, V. Badilita, A. Caragea, M. Tarcolea, Electrochemical deposition and microstructural characterization of AlCrFeMnNi and AlCrCuFeMnNi high entropy alloy thin films, *Appl. Surf. Sci.* 358 (2015) 533–539, <https://doi.org/10.1016/j.apsusc.2015.07.142>.
- [21] A.H. Phakatkhar, M.T. Saray, M.G. Rasul, L.V. Sorokina, T.G. Ritter, T. Shokuhfar, R. Shahbazian-Yassar, Ultrafast synthesis of high entropy oxide nanoparticles by flame spray pyrolysis, *Langmuir* 37 (2021) 9059–9068, <https://doi.org/10.1021/acs.langmuir.1c01105>.
- [22] D. Wu, K. Kusada, T. Yamamoto, T. Toriyama, S. Matsumura, S. Kawaguchi, Y. Kubota, H. Kitagawa, Platinum-group-metal high-entropy-alloy nanoparticles, *J. Am. Chem. Soc.* 142 (2020) 13833–13838, <https://doi.org/10.1021/jacs.0c04807>.
- [23] F. Xing, J. Ma, K.I. Shimizu, S. Furukawa, High-entropy intermetallics on ceria as efficient catalysts for the oxidative dehydrogenation of propane using CO₂, *Nat. Commun.* 13 (2022) 5065, <https://doi.org/10.1038/s41467-022-32842-8>.
- [24] T. Li, Y. Yao, B.H. Ko, Z. Huang, Q. Dong, J. Gao, W. Chen, J. Li, S. Li, X. Wang, R. Shahbazian-Yassar, F. Jiao, L. Hu, Carbon-supported high-entropy oxide nanoparticles as stable electrocatalysts for oxygen reduction reactions, *Adv. Funct. Mater.* 31 (2021), <https://doi.org/10.1002/adfm.202010561>.
- [25] S. Sun, C. Dai, P. Zhao, S. Xi, Y. Ren, H.R. Tan, P.C. Lim, M. Lin, C. Diao, D. Zhang, C. Wu, A. Yu, J.C.J. Koh, W.Y. Lieu, D.H.L. Seng, L. Sun, Y. Li, T.L. Tan, J. Zhang, Z. J. Xu, Z.W. Seh, Spin-related Cu-Co pair to increase electrochemical ammonia generation on high-entropy oxides, *Nat. Commun.* 15 (2024) 260, <https://doi.org/10.1038/s41467-023-44587-z>.
- [26] R.R. Kitzbaer, F.M. Dos Santos Vieira, I. Dabo, Z. Mao, R.E. Schaak, Band gap narrowing in a high-entropy spinel oxide semiconductor for enhanced oxygen evolution catalysis, *J. Am. Chem. Soc.* 145 (2023) 6753–6761, <https://doi.org/10.1021/jacs.2c12887>.
- [27] S. Akrami, Y. Murakami, M. Watanabe, T. Ishihara, M. Arita, M. Fuji, K. Edalati, Defective high-entropy oxide photocatalyst with high activity for CO₂ conversion, *Appl. Catal., B* 303 (2022) 120896, <https://doi.org/10.1016/j.apcatb.2021.120896>.
- [28] H. Xu, Z. Zhang, J. Liu, C.L. Do-Thanh, H. Chen, S. Xu, Q. Lin, Y. Jiao, J. Wang, Y. Wang, Y. Chen, S. Dai, Entropy-stabilized single-atom Pd catalysts via high-entropy fluorite oxide supports, *Nat. Commun.* 11 (2020) 3908, <https://doi.org/10.1038/s41467-020-17738-9>.
- [29] J. Zhao, J. Bao, S. Yang, Q. Niu, R. Xie, Q. Zhang, M. Chen, P. Zhang, S. Dai, Exsolution–dissolution of supported metals on high-entropy Co₃MnNiCuZnO_x: toward sintering-resistant catalysis, *ACS Catal.* 11 (2021) 12247–12257, <https://doi.org/10.1021/acscatal.1c03228>.
- [30] T. Li, Y. Yao, Z. Huang, P. Xie, Z. Liu, M. Yang, J. Gao, K. Zeng, A.H. Brozena, G. Pastel, M. Jiao, Q. Dong, J. Dai, S. Li, H. Zong, M. Chi, J. Luo, Y. Mo, G. Wang, C. Wang, R. Shahbazian-Yassar, L. Hu, Denary oxide nanoparticles as highly stable catalysts for methane combustion, *Nat. Catal.* 4 (2021) 62–70, <https://doi.org/10.1038/s41929-020-00554-1>.
- [31] S. Hou, X. Ma, Y. Shu, J. Bao, Q. Zhang, M. Chen, P. Zhang, S. Dai, Self-regeneration of supported transition metals by a high entropy-driven principle, *Nat. Commun.* 12 (2021) 5917, <https://doi.org/10.1038/s41467-021-26160-8>.
- [32] J. Huang, W. Liu, Y. Yang, B. Liu, High-Performance Ni-Fe Redox Catalysts for Selective CH₄ to Syngas Conversion via Chemical Looping, *ACS Catal.* 8 (2018) 1748–1756, <https://doi.org/10.1021/acscatal.7b03964>.
- [33] X. Zhang, Y. Xu, Y. Liu, L. Niu, Y. Diao, Z. Gao, B. Chen, J. Xie, M. Bi, M. Wang, D. Xiao, D. Ma, C. Shi, A novel Ni–MoC_xO_y interfacial catalyst for syngas production via the chemical looping dry reforming of methane, *Chem* 9 (2023) 102–116, <https://doi.org/10.1016/j.chempr.2022.09.007>.
- [34] Q. Yang, L. Chen, N. Jin, Y. Zhu, J. He, P. Zhao, C. Huang, L. Wei, X. Ma, X. Wang, Boosted carbon resistance of ceria-hexaaluminate by in-situ formed CeFe_xAl_{1-x}O₃ as oxygen pool for chemical looping dry reforming of methane, *Appl. Catal. B* 330 (2023) 122636, <https://doi.org/10.1016/j.apcatb.2023.122636>.
- [35] R. Liu, X.H. Zhang, T. Liu, X. Yao, Z.J. Zhao, C.L. Pei, J.L. Gong, Dynamic oxygen migration and reaction over ceria-supported nickel oxides in chemical looping partial oxidation of methane, *Appl. Catal., B* 328 (2023) 122478, <https://doi.org/10.1016/j.apcatb.2023.122478>.
- [36] W. Chang, Y. Gao, J. He, X. Xia, C. Huang, Y. Hu, W. Xu, B. Jiang, Y. Han, Y. Zhu, X. Wang, Asymmetric coordination activated lattice oxygen in perovskite ferrites for selective anaerobic oxidation of methane, *J. Mater. Chem. A* 11 (2023) 4651–4660, <https://doi.org/10.1039/d2ta09187a>.
- [37] K. Zhao, A.Q. Zheng, H.B. Li, F. He, Z. Huang, G.Q. Wei, Y. Shen, Z.L. Zhao, Exploration of the mechanism of chemical looping steam methane reforming using double perovskite-type oxides La_{1.6}Sr_{0.4}FeCoO₆, *Appl. Catal. B* 219 (2017) 672–682, <https://doi.org/10.1016/j.apcatb.2017.08.027>.
- [38] X. Xia, W. Chang, S. Cheng, C. Huang, Y. Hu, W. Xu, L. Zhang, B. Jiang, Z. Sun, Y. Zhu, X. Wang, Oxygen activity tuning via FeO₆ octahedral tilting in perovskite ferrites for chemical looping dry reforming of methane, *ACS Catal.* 12 (2022) 7326–7335, <https://doi.org/10.1021/acscatal.2c00920>.
- [39] F. Wang, P. Zou, Y. Zhang, W. Pan, Y. Li, L. Liang, C. Chen, H. Liu, S. Zheng, Activating lattice oxygen in high-entropy LDH for robust and durable water oxidation, *Nat. Commun.* 14 (2023) 6019, <https://doi.org/10.1038/s41467-023-41706-8>.
- [40] J. Ni, Z.P. Shi, Y.B. Wang, J.H. Yang, H.X. Wu, P.B. Wang, K. Li, M.L. Xiao, C.P. Liu, W. Xing, Suppressing the lattice oxygen diffusion via high-entropy oxide construction towards stabilized acidic water oxidation, *Nano Res.* 17 (2024) 1107–1113, <https://doi.org/10.1007/s12274-023-5913-6>.
- [41] X.J. Wang, Y.F. Gao, E. Krzystowczyk, S. Ifikhar, J. Dou, R.X. Cai, H.Y. Wang, C. Y. Ruan, S. Ye, F.X. Li, High-throughput oxygen chemical potential engineering of perovskite oxides for chemical looping applications, *Energy Environ. Sci.* 15 (2022) 1512–1528, <https://doi.org/10.1039/d1ee02889h>.
- [42] Y.J. Han, M. Tian, C.J. Wang, T. Zong, X.D. Wang, High-entropy spinel oxide (Fe_{0.2}Mg_{0.2}Mn_{0.1}Al_{0.3}Cr_{0.2})₃O₄ as a highly active and stable redox material for methane driven solar thermochemical water splitting, *Appl. Catal. B* 339 (2023) 123096, <https://doi.org/10.1016/j.apcatb.2023.123096>.
- [43] K.C. Pitike, K.C. Santosh, M. Eisenbach, C.A. Bridges, V.R. Cooper, Predicting the phase stability of multicomponent high-entropy compounds, *Chem. Mater.* 32 (2020) 7507–7515, <https://doi.org/10.1021/acs.chemmater.0c02702>.
- [44] L. Spiridigliozzi, G. Dell’Aglia, E. Callone, S. Dire, R. Camprostrini, P. Bettotti, M. Bortolotti, G. Speranza, V.M. Sglavo, M. Biesuz, A structural and thermal investigation of Li-doped high entropy (Mg, Co, Ni, Cu, Zn)O obtained by coprecipitation, *J. Alloy. Compd.* 927 (2022) 166933, <https://doi.org/10.1016/j.jallcom.2022.166933>.
- [45] A.C. Larson, R.B. Von Dreele, *Generalized Structure Analysis System*, University of California, 1988.
- [46] Y. Du, Y. Zhu, S. Xi, P. Yang, H.O. Moser, M.B. Breese, A. Borgna, XAFCA: a new XAFS beamline for catalysis research, *J. Synchrotron Radiat.* 22 (2015) 839–843, <https://doi.org/10.1107/S1600577515002854>.
- [47] B. Ravel, M. Newville, ATHENA, ARTEMIS, HEPHAESTUS: data analysis for X-ray absorption spectroscopy using IFEFFIT, *J. Synchrotron Radiat.* 12 (2005) 537–541, <https://doi.org/10.1107/S0909049505012719>.
- [48] Q.W.H. Fan, C.D. Huang, S.B. Xi, Y. Yan, J.J. Huang, S. Saqline, L.G. Tao, Y.H. Dai, A. Borgna, X.D. Wang, W. Liu, Breaking the stoichiometric limit in oxygen-carrying capacity of Fe-based oxygen carriers for chemical looping combustion using the Mg-Fe-O solid solution system, *ACS Sustain. Chem. Eng.* 10 (2022) 7242–7252, <https://doi.org/10.1021/acssuschemeng.2c00271>.
- [49] S. Shah, M. Xu, X. Pan, K.L. Gilliard-Abdulaziz, Exsolution of embedded Ni–Fe–Co nanoparticles: implications for dry reforming of methane, *ACS Appl. Nano Mater.* 4 (2021) 8626–8636, <https://doi.org/10.1021/acsnm.1c02268>.
- [50] A. Tsoukalou, Q. Imtiaz, S.M. Kim, P.M. Abdal, S. Yoon, C.R. Müller, Dry-reforming of methane over bimetallic Ni–M/La₂O₃ (M = Co, Fe): the effect of the rate of La₂O₂CO₃ formation and phase stability on the catalytic activity and stability, *J. Catal.* 343 (2016) 208–214, <https://doi.org/10.1016/j.jcat.2016.03.018>.
- [51] L.P. Merkouri, A.I. Paksoy, T. Ramirez Reina, M.S. Duyar, The need for flexible chemical synthesis and how dual-function materials can pave the way, *ACS Catal.* 13 (2023) 7230–7242, <https://doi.org/10.1021/acscatal.3c00880>.
- [52] M. Rydén, D. Jing, M. Källén, H. Leion, A. Lyngfelt, T. Mattisson, CuO-based oxygen-carrier particles for chemical-looping with oxygen uncoupling – experiments in batch reactor and in continuous operation, *Ind. Eng. Chem. Res.* 53 (2014) 6255–6267, <https://doi.org/10.1021/ie4039983>.
- [53] S.K. Maity, M.S. Rana, B.N. Srinivas, S.K. Bej, G.M. Dhar, T.S.R.P. Rao, Characterization and evaluation of ZrO supported hydrotreating catalysts, *J. Mol. Catal. A: Chem.* 153 (2000) 121–127, [https://doi.org/10.1016/S1381-1169\(99\)00311-8](https://doi.org/10.1016/S1381-1169(99)00311-8).

- [54] S.A. Theofanidis, V.V. Galvita, H. Poelman, G.B. Marin, Enhanced carbon-resistant dry reforming Fe-Ni catalyst: role of Fe, *ACS Catal.* 5 (2015) 3028–3039, <https://doi.org/10.1021/acscatal.5b00357>.
- [55] T.T. Zhang, Z.X. Liu, Y.A. Zhu, Z.C. Liu, Z.J. Sui, K.K. Zhu, X.G. Zhou, Dry reforming of methane on Ni-Fe-MgO catalysts: Influence of Fe on carbon-resistant property and kinetics, *Appl. Catal. B* 264 (2020) 118497, <https://doi.org/10.1016/j.apcatb.2019.118497>.
- [56] D.L. Li, S.P. Xu, K. Song, C.Q. Chen, Y.Y. Zhan, L.L. Jiang, Hydrotalcite-derived Co/Mg(Al)O as a stable and coke-resistant catalyst for low-temperature carbon dioxide reforming of methane, *Appl. Catal. A* 552 (2018) 21–29, <https://doi.org/10.1016/j.apcata.2017.12.022>.
- [57] P. Munster, H.J. Grabke, Kinetics of the steam reforming of methane with iron, nickel, and iron-nickel alloys as catalysts, *J. Catal.* 72 (1981) 279–287, [https://doi.org/10.1016/0021-9517\(81\)90010-5](https://doi.org/10.1016/0021-9517(81)90010-5).
- [58] N.S. Yüzbaşı, A. Armutlulu, T. Huthwelker, P.M. Abdala, C.R. Müller, Na- β -Al₂O₃ stabilized Fe₂O₃ oxygen carriers for chemical looping water splitting: correlating structure with redox stability, *J. Mater. Chem. A* 10 (2022) 10692–10700, <https://doi.org/10.1039/d1ta10507h>.
- [59] B. Jin, K. Wei, T. Ouyang, Y. Fan, H. Zhao, H. Zhang, Z. Liang, Chemical looping CO₂ capture and in-situ conversion: Fundamentals, process configurations, bifunctional materials, and reaction mechanisms, *Appl. Energy Combust. Sci.* 16 (2023), <https://doi.org/10.1016/j.jaecs.2023.100218>.
- [60] Z. Ma, D. Zeng, S. Zhang, R. Xiao, Effect of supports on the redox performance of NiFe₂O₄ in a chemical looping process, *Energy Technol.* 7 (2019), <https://doi.org/10.1002/ente.201900374>.
- [61] P.E. Quintard, P. Barbéris, A.P. Mirgorodsky, T. Merle-Méjean, Comparative lattice-dynamical study of the raman spectra of monoclinic and tetragonal phases of zirconia and hafnia, *J. Am. Ceram. Soc.* 85 (2004) 1745–1749, <https://doi.org/10.1111/j.1151-2916.2002.tb00346.x>.
- [62] O.N. Shebanova, P. Lazor, Raman spectroscopic study of magnetite (FeFe₂O₄): a new assignment for the vibrational spectrum, *J. Solid State Chem.* 174 (2003) 424–430, [https://doi.org/10.1016/s0022-4596\(03\)00294-9](https://doi.org/10.1016/s0022-4596(03)00294-9).
- [63] A. Parmaliana, F. Arena, F. Frusteri, N. Giordano, Temperature-programmed reduction study of NiO–MgO interactions in magnesia-supported Ni catalysts and NiO–MgO physical mixture, *J. Chem. Soc. Faraday Trans. 86* (1990) 2663–2669, <https://doi.org/10.1039/ft9908602663>.
- [64] G.U. Kulkarni, G. Sankar, C.N.R. Rao, Analysis of exafs data of complex-systems, *Z. Phys. B* 73 (1989) 529–537, <https://doi.org/10.1007/Bf01319382>.
- [65] R.B. Gregor, F.W. Lytle, Morphology of supported metal clusters: determination by EXAFS and chemisorption, *J. Catal.* 63 (1980) 476–486, [https://doi.org/10.1016/0021-9517\(80\)90102-5](https://doi.org/10.1016/0021-9517(80)90102-5).
- [66] T. Kim, B.H. Song, A.J.G. Lunt, G. Cibin, A.J. Dent, L. Lu, A.M. Korsunsky, Operando X-ray absorption spectroscopy study of atomic phase reversibility with wavelet transform in the lithium-rich manganese based oxide cathode, *Chem. Mater.* 28 (2016) 4191–4203, <https://doi.org/10.1021/acs.chemmater.6b00522>.
- [67] Z. Su, X. Li, W. Si, L. Artiglia, Y. Peng, J. Chen, H. Wang, D. Chen, J. Li, Probing the actual role and activity of oxygen vacancies in toluene catalytic oxidation: evidence from in situ XPS/NEXAFS and DFT + *U* calculation, *ACS Catal.* 13 (2023) 3444–3455, <https://doi.org/10.1021/acscatal.3c00333>.
- [68] D. Wang, Q. Li, C. Han, Q. Lu, Z. Xing, X. Yang, Atomic and electronic modulation of self-supported nickel-vanadium layered double hydroxide to accelerate water splitting kinetics, *Nat. Commun.* 10 (2019) 3899, <https://doi.org/10.1038/s41467-019-11765-x>.
- [69] N. Pauly, F. Yubero, F.J. García-García, S. Tougaard, Quantitative analysis of Ni 2p photoemission in NiO and Ni diluted in a SiO₂ matrix, *Surf. Sci.* 644 (2016) 46–52, <https://doi.org/10.1016/j.susc.2015.09.012>.
- [70] K.J. Gaskell, A. Starace, M.A. Langell, Zn_xNi_{1-x}O rocksalt oxide surfaces: novel environment for Zn²⁺ and its effect on the NiO band structure, *J. Phys. Chem. C* 111 (2007) 13912–13921, <https://doi.org/10.1021/jp073590x>.